Journal of Physics D: Applied Physics

PAPER

Nanoscale amorphous interfaces in phase-change memory materials: structure, properties and design

To cite this article: Xue-Peng Wang *et al* 2020 *J. Phys. D: Appl. Phys.* **53** 114002

View the article online for updates and enhancements.

IOP ebooks™

Bringing you innovative digital publishing with leading voices to create your essential collection of books in STEM research.

Start exploring the collection - download the first chapter of every title for free.

This content was downloaded from IP address 202.198.26.182 on 04/01/2020 at 00:53

IOP Publishing Journal of Physics D: Applied Physics
J. Phys. D: Appl. Phys. **53** (2020) 114002 (8pp) https://doi.org/10.1088/1361-6463/ab5d81

Nanoscale amorphous interfaces in phase-change memory materials: structure, properties and design

Xue-Peng Wang[1], Yu-Ting Liu[1], Yong-Jin Chen[2,3], Nian-Ke Chen[1] and Xian-Bin Li[1]

[1] State Key Laboratory of Integrated Optoelectronics, College of Electronic Science and Engineering, Jilin University, Changchun 130012, People's Republic of China
[2] Institute of Microstructure and Property of Advanced Materials, Beijing University of Technology, Beijing 100124, People's Republic of China
[3] Center for High Pressure Science and Technology Advanced Research (HPSTAR), Beijing 100094, People's Republic of China

E-mail: chennianke@jlu.edu.cn or lixianbin@jlu.edu.cn

Received 12 September 2019, revised 31 October 2019
Accepted for publication 29 November 2019
Published 3 January 2020

Abstract

Phase-change memory (PCM) is one of the emerging technologies for the next generation of electric and optical memories. In a typical PCM device, a nanoscale amorphous interface can usually be observed. These nano amorphous interfaces are crucial because they could affect the phase transition characteristics of PCM materials, especially when the PCM devices are scaling down. In this work, according to results of our previous first-principles calculations and transmission electron microscope characterizations, we revisit the effects of three typical nano amorphous interfaces of PCM materials between different phases. We conclude that the bonding network and electronic features of the PCM material in these interfaces will be changed significantly depending on the material next to it. Different types of interface could either enhance the stability of amorphous (i.e. amorphous Si/amorphous Sb_2Te_3 interface) and metastable crystalline phases (i.e. amorphous GeTe/cubic Sb_2Te_3 interface) or promote crystallization (i.e. amorphous and crystalline $Ge_2Sb_2Te_5$ interface) of the PCM materials. Therefore, a nano amorphous interface can be used to control the performance of PCM devices, such as data retention ability and crystallization speed. The present work also offers a feasible way to design novel nanoscale PCM materials based on the interface effects.

Keywords: phase-change memory material, amorphous interface, data retention, crystallization

(Some figures may appear in colour only in the online journal)

1. Introduction

The reversible and rapid phase transition phenomenon of phase-change memory (PCM) materials was observed as early as 1968 by Sir Ovshinsky [1]. These materials have attracted much attention for use in non-volatile electrical and optical data storage [2–6], especially in the past decade. The phase transition between their amorphous and crystalline phases can provide a large contrast in electrical and optical properties, such as resistance and reflectivity [7–9]. Nowadays, PCM materials are also used in emerging new computational architecture, such as storage class memory [3] and brain-inspired computing [10–13].

Interfaces are ubiquitous in a typical PCM device, for example the interfaces between a PCM material and the substrate or electrode [14, 15]. There are also interfaces between different phases or components of the PCM material itself. For example, due to partial melting or phase change in a typical mushroom-type PCM cell [16], interfaces exist between amorphous and crystalline parts of the PCM material. In

 © 2020 IOP Publishing Ltd Printed in the UK

recent years, because of this partial and stepwise phase-change ability, PCM materials have been employed to emulate the behavior of biological neurons, and thus applied in brain-inspired computing [17]. Apart from partial phase change, for a special class of PCM materials, such as C-doped $Ge_2Sb_2Te_5$ (GST) [18] and SiSbTe [19, 20], nanoscale phase separation usually occurs. Generally, such phase separation will lead to the formation of interfaces between non-PCM materials (i.e. C or Si) and PCM materials (i.e. GST or Sb_2Te_3). These interfaces are crucial for the performance of PCM devices because of their different structure and property compared with the bulk phase. In addition, as PCM devices scale down, the interface effect will be more significant as the proportion of interface increases [21]. To date, some new PCM material components have been proposed based on the interface effect. For instance, the GeTe/Sb_2Te_3 superlattice, known as an interfacial phase-change material (iPCM) [22, 23], exhibits a very fast phase-change speed and quite low power consumption. Other examples are transition metal-doped PCM materials such as TiSbTe and ScSbTe [24, 25]. The stable $TiTe_2$ slab motifs in TiSbTe could accelerate the crystallization (or SET) speed of the amorphous parts through the interfaces between them [26]. Therefore, investigation of interface effects is a key issue for improving performance and developing new designs for PCM materials and devices.

In this work, we revisit the effects of nano amorphous interfaces on the structure and properties of PCM materials based on our previous first-principles density functional theory (DFT) [27] studies as well as transmission electron microscope (TEM) characterizations for PCM applications. Three kinds of typical amorphous interfaces in PCM materials, including amorphous Si/amorphous Sb_2Te_3 (amorphous–amorphous) interfaces [20], amorphous/crystalline GST (homogeneous amorphous–crystalline) interfaces [28] and amorphous GeTe/cubic Sb_2Te_3 (heterogeneous amorphous–crystalline) interfaces [29], are studied. We conclude that amorphous Si could stabilize amorphous Sb_2Te_3 by changing its bonding network and inhibiting its crystallization process. In a homogeneous amorphous–crystalline GST interface, the crystalline part could act as a template to accelerate crystallization of the amorphous part. Finally, by TEM investigation, metastable cubic Sb_2Te_3 is found to be stabilized by amorphous GeTe in amorphous GeTe/Sb_2Te_3 superlattice-like films. These results indicate that nano amorphous interfaces can be used to control aspects of performance such as data retention and SET speed of PCM materials and also the PCM devices based on them.

2. Methods

Our DFT calculations are performed within the projected augmented wave (PAW) formalism [30], as implemented in VASP codes [31]. The Perdew–Burke–Ernzerhof (PBE) functional [32] is used to describe the electronic exchange–correlation interaction. In the *ab initio* molecular dynamic (MD) simulations we use the NVT canonical ensemble, in which a Nośe thermostat is used to control the temperature [33]. For analysis of the bonding structure, the cutoff for bond length is 1.2 times the sum of covalent radii between any two atoms.

For amorphous Si and amorphous Sb_2Te_3 interfaces, as described in our previous work [20], the model is built based on a $4 \times 2 \times 1$ supercell of hexagonal Sb_2Te_3. Half of the Sb and Te atoms are replaced by Si atoms with the experimental density of amorphous Si [34]. To build the interface structure, the Sb_2Te_3 part is locked and the Si part is melted at 3000 K, equilibrated at 1900 K and finally quenched to 300 K. After that, the Si part is locked and the amorphization of Sb_2Te_3 is also carried out by melting at 3000 K, equilibrating at 1000 K and finally quenching to 300 K. The MD simulations above are run for 6 ps with a time step of 1 fs for Si and 3 fs for Sb_2Te_3. Finally, the two parts are annealed together at 300 K for 9 ps to obtain the amorphous Si and amorphous Sb_2Te_3 interface structure (including 96 Si, 24 Sb and 36 Te atoms) shown in figure 1(a). For comparison a bulk amorphous Sb_2Te_3 structure is also obtained by the same melt-quenching method. An energy cutoff of 270 eV and *K*-point set of $2 \times 2 \times 1$ are used for the MD calculations above.

The amorphous and crystalline GST interface is built based on a vacancy-ordered cubic (VOC) GST model [28]. The VOC phase has vacancy-ordered layers, ensuring that partial melting priority occurs around these vacancy-ordered layers. Melting of VOC GST is performed at 1300 K for 6 ps followed by rapid quenching to 300 K. Then the interface structure shown in figure 3(a) is obtained after further maintenance at 300 K for 39 ps. Therefore, the amorphous part of the amorphous and crystalline GST interface is rich in vacancies or voids [28]. As described in our previous work [28], the amorphous and crystalline GST interface model has a density of 6.02 g cm^{-3} and contains 38 Ge, 38 Sb and 96 Te atoms. For the MD calculations in this model, the plane-wave energy cutoff is 200 eV and a single *K*-point is used.

For the energy calculations shown in figure 5, the models for amorphous, cubic and hexagonal phases of Sb_2Te_3 contain 60 (24 Sb and 36 Te), 53 (21 Sb and 32 Te) and 5 (2 Sb and 3 Te) atoms, respectively. An energy cutoff of 230 eV is used. In the experiment in [29], the amorphous GeTe and Sb_2Te_3 superlattice-like film were deposited on a SiO_2/Si (1 0 0) substrate using the radiofrequency sputtering method. The cross-sectional sample for TEM investigations was prepared by a combination of Ga focussed ion beam (FIB) and Ar low-energy ion beam milling. The TEM investigations were performed on a Cs-corrected FEI Titan G2 80-300 microscope with super x-ray energy dispersive spectrometry (EDS).

3. Results and discussions

First we study the amorphous–amorphous interface between Si and Sb_2Te_3 (iST). As mentioned above, this interface has been observed in SiSbTe PCM material due to the nanoscale phase separation [19]. It is recognized that amorphous Si has a typical sp^3 hybrid bonding network and Si atoms are connected with each other by covalent bonds. Atoms in crystalline PCM materials usually form unique resonant or metavalent

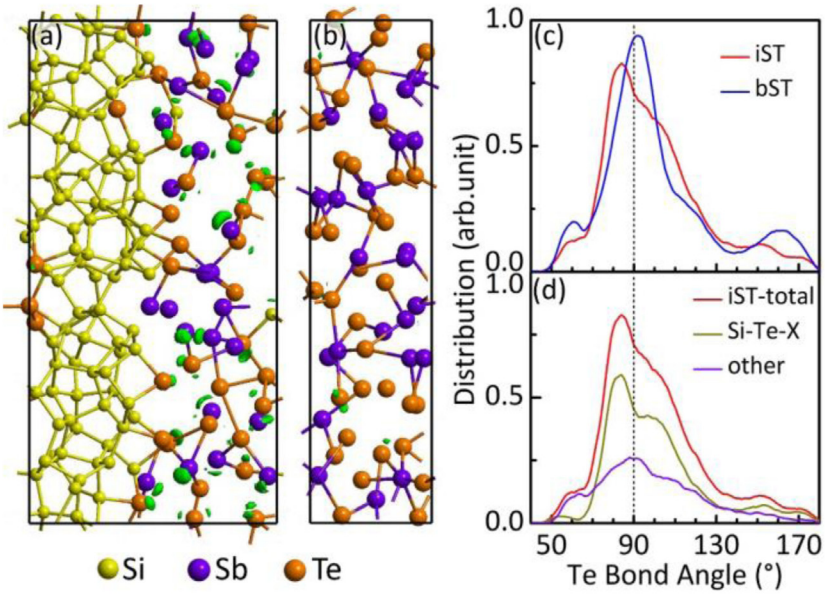

Figure 1. Structure of (a) the amorphous Si and amorphous Sb_2Te_3 interface (iST) and (b) bulk amorphous Sb_2Te_3 (bST) with an isosurface of 0.92 in the ELF (green dots). For comparison, only the ELF distribution in the Sb_2Te_3 part is shown. Atom color coding: yellow for Si, purple for Sb, orange for Te. (c) Te bond angle distribution in amorphous Sb_2Te_3 of iST and bST, respectively. (a)–(c) Reproduced from [20] with permission of The Royal Society of Chemistry. (d) Partial bond angle distribution of Te in iST. The symbol X can be any type of atom.

bonds [35, 36] by p electrons, and these electrons are more delocalized than those in covalent bonds. The delocalized feature of electrons is also maintained to a certain degree in amorphous PCM materials [37]. This result can be confirmed by the electron localization function (ELF) [38] distribution. As shown in our previous work [20], figures 1(a) and (b) display the ELF = 0.92 isosurface to reflect the distribution of highly localized electrons which are usually observed in strong covalent bonds and lone pairs. Bulk amorphous Sb_2Te_3 (bST) has few highly localized electrons, as described in figure 1(b), while the amorphous Sb_2Te_3 in iST exhibits more localized electrons as they are affected by amorphous Si (see figure 1(a) [20]). Since the change in electronic structure often affects the bonding network, we analyze and compare the bond angle distribution in iST and bST. As pointed out in [20], amorphous Si mainly affects the bond angle distribution of Te (see figure 1(c)). In bST, most of the Te atoms have a 90° bond angle which is the p orbital bonding feature, while in iST the main peak of Te bond angle distribution shifts to about 80°. The Te bond angle in iST is also more distributed between 100° and 120° compared with that of bST. To find the origins for these new bond angles, in figure 1(d) we further divide the Te bond angle distribution into two parts according to its connection. One of these is the Si–Te–X bond angle, where X stands for any type of atom, so Si–Te–X are the Te atoms that bond with at least one Si atom. The other is the Te-centered bond angle that contains no Si atoms. Obviously, all the new bond angles appearing in iST are related to Si. On the contrary, the Te bond angles without any Si show a main peak at 90°. In addition, according to the bond angle and local order parameter [39] distribution analysis in our previous work [20], amorphous Si has little impact on the bonding configuration of Sb in iST. Turning to the ELF distribution shown in figure 1(a), the localized electrons in iST are in the form of lone pairs according to their cap-like shape distribution area. Therefore, through the Si–Te bonds, amorphous Si modifies the bonding feature of Te from p-bonding (in bST) to sp^3 hybridization to a certain degree (in iST) [20]. This results in a distortion of the Te bonding network, and presents a barrier for the amorphous-to-crystalline phase transition of iST.

To test whether crystallization of iST will be inhibited by amorphous Si, two recrystallization MD simulations of iST and bST at 600 K are carried out [20]. Figures 2(a) and (b) display the pair correlation function (PCF) evolution of iST and bST, respectively. At 0 ps, both the PCFs converge to 1 in the range of $r > 7$ Å, which is a feature of the amorphous phase. The PCF for bST shows visible peaks and valleys in the $r > 7$ Å region after 24 ps. This implies that the structure has a long-range order after 24 ps in the simulation. There are almost no significant changes in the PCF of iST during the whole recrystallization on the same time scale, so it stays in the amorphous phase. This can be confirmed by the evolution of electronic properties during recrystallization. Figures 2(c) and (d) show the calculated imaginary part of the dielectric constant (ε_2) of iST and bST at different times. Consistent with the structural evolution, ε_2 of iST remains almost unchanged while ε_2 of bST shows a significant increase at 12 ps and reaches a maximum after 24 ps. Note that the calculated value of ε_2 may have deviated from the experimental one, but it could confirm that the evolution of electronic properties exactly matches the structural evolution. Therefore, crystallization of iST is suppressed by amorphous Si through their interface. This also means that amorphous Si can enhance the stability of amorphous Sb_2Te_3. In fact, $Si_{3.5}Sb_2Te_3$ has a 10-year data retention temperature of 412 K, which is higher than that of GST (364 K) [19].

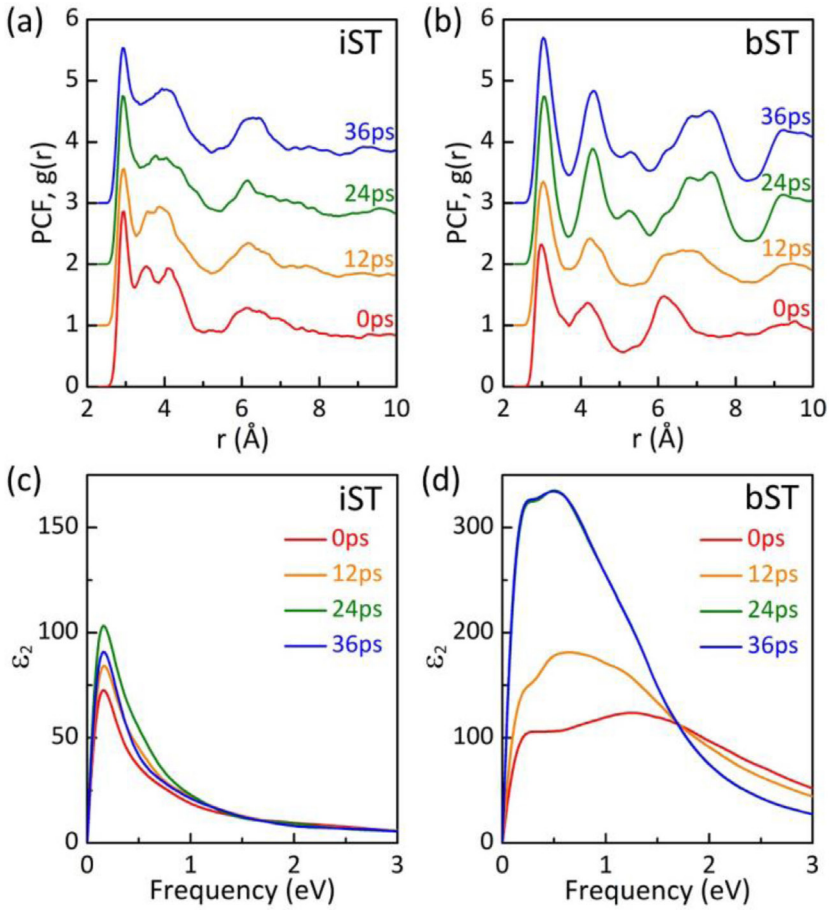

Figure 2. PCF and the calculated imaginary part of dielectric constant (ε_2) of (a), (c) iST and (b), (d) bST during recrystallization in the models of figure 1. The Si atoms were removed when calculating the ε_2 of iST.

In summary, amorphous non-PCM materials with non-p orbital bonding characteristics (such as strong covalent sp^3 bonding materials like Si and C) could affect the electronic properties and lead to structural distortion of amorphous PCM materials through the interface. The structural distortion raises the barrier of the amorphous-to-crystalline phase transition. Based on this mechanism, amorphous non-PCM material/amorphous PCM material interfaces can be employed to enhance the data retention ability of PCM materials and devices.

Next, the homogeneous amorphous–crystalline interface between amorphous and crystalline GST is investigated. We know that GST has a rock-salt cubic crystalline phase. Cubic GST contains 20% cation vacancies which have a random distribution [40]. In fact, GST also has a VOC phase in which vacancies are highly ordered in the form of vacancy layers in (1 1 1) planes. The VOC phase that has been observed by scanning transmission electron microscopy can be obtained by further annealing the normal cubic (random vacancy) phase at a higher temperature [40, 41]. Furthermore, as demonstrated in our previous work, melting (or amorphization) of the VOC GST starts around the vacancy layers [40]. This makes melting of the VOC GST controllable and offers the opportunity to build an amorphous–crystalline GST interface by partial melting. The interface structure is shown in figure 3(a) [28]. However, because the amorphous part is obtained from the region around the vacancy layer of the VOC phase it contains more vacancies or voids than bulk amorphous GST (bGST), as confirmed in our previous work [28]. Because the amorphous part of the interface structure (iGST) is more complex and unclear, we mainly focus on the structure and electronic properties of this part. In bGST, most of the atoms have a defective octahedral bonding configuration due to the p-bonding feature. However, some Ge atoms are found to be tetrahedrally coordinated [39, 42]. These Ge atoms are believed to be related to the stability of the amorphous phase [43]. Meanwhile, the tetrahedral to octahedral bonding configuration transformation of Ge is one of the mechanisms proposed for the phase switching of GST [42, 44]. As pointed out in previous works [28, 39], the proportion of tetrahedral Ge can be obtained from the local order parameter q. This parameter is usually used to identify local octahedral and tetrahedral bonding configurations. The definition of q is

$$q = 1 - \frac{3}{8}\sum_{i>k}\left(\frac{1}{3} + cos\theta_{ijk}\right)^2$$

where the sum of the bond angles runs over pairs of atoms bonded to a central atom j [39, 45]. The proportion of tetrahedral Ge is estimated by integrating the q of four coordinated Ge atoms in the range of 0.8–1.0 [28, 39]. Figure 3(b) shows

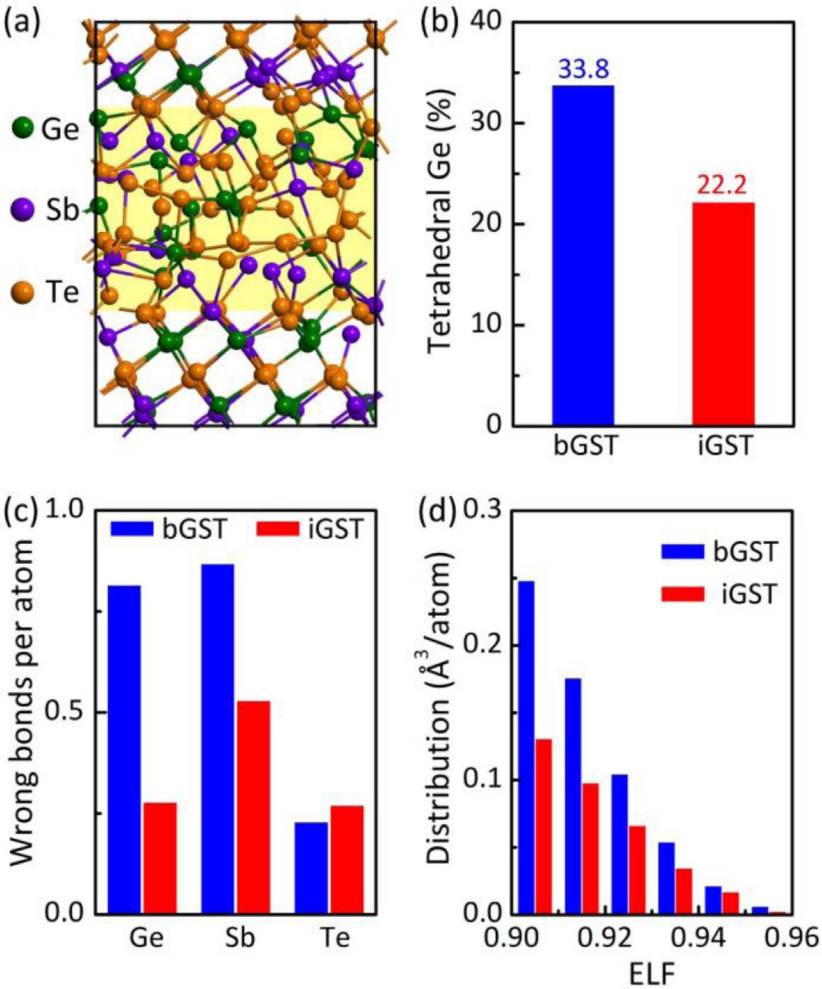

Figure 3. (a) Structure of the amorphous and crystalline GST interface. Atom color coding: green for Ge, purple for Sb, orange for Te. The yellow shaded area is the amorphous part (iGST). Reprinted from [28], Copyright 2017, with permission from Elsevier. (b) Percentage of Ge with tetrahedral bond configuration. (c) Wrong bonds per atom of Ge, Sb and Te. (d) The integrated volume occupied by electrons with different ELFs in bGST and iGST, respectively.

that only 22.2% of the Ge atoms have a tetrahedral bonding configuration in iGST, which is lower than in bGST (33.8%) [28]. In addition, we also find the iGST have fewer wrong (homogeneous) bonds (the Ge–Sb bond is also classified as a wrong bond) [46] than bGST. As displayed in figure 3(c), despite Te having a few more wrong bonds, both Ge and Sb form fewer wrong bonds in iGST. This means the iGST is more chemically ordered than bGST. As well as the bonding structure, comparison of the electronic structure between iGST and bGST is also performed by analysis of the ELF. Figure 3(d) displays the estimated volume occupied by electrons with ELF in the range 0.9–0.96 to reflect the highly localized electron distribution. Obviously, iGST has fewer localized electrons than bGST. In a word, iGST has weaker amorphous phase features (in terms of tetrahedral Ge, wrong bonds and localized electrons) because of the proximity effect of the crystalline part via the homogeneous amorphous–crystalline interface [28, 47]. As mentioned above, iGST here has more voids than bGST [28]. This may also have some effect on the above results.

Since iGST has weaker amorphous phase features it may have poor stability and be easy to crystallize. To examine this, recrystallization of iGST at 600 K is carried out. For comparison, recrystallization of bGST is also performed at the same temperature and on the same time scale [28]. Figure 4 shows the structural evolution of the two phases during recrystallization. From the structure of iGST at 0 ps and 30 ps we can observe that recrystallization begins at the interface. The crystalline part acts as a nucleus and gradually grows into the amorphous part. After 60 ps, iGST transforms into an ordered crystalline phase. In contrast, bGST maintains the amorphous features after 90 ps. The recrystallization process verifies that in homogeneous amorphous and crystalline interface structure, the amorphous part becomes unstable and has a faster crystallization speed. The larger number of voids in iGST could also accelerate the crystallization because they offer space for atomic rearrangement [28, 48]. However, the crystalline template should play a more important role in the fast crystallization process. In 2015, Ronneberger *et al* investigated the growth process from a normal amorphous (not rich in voids)

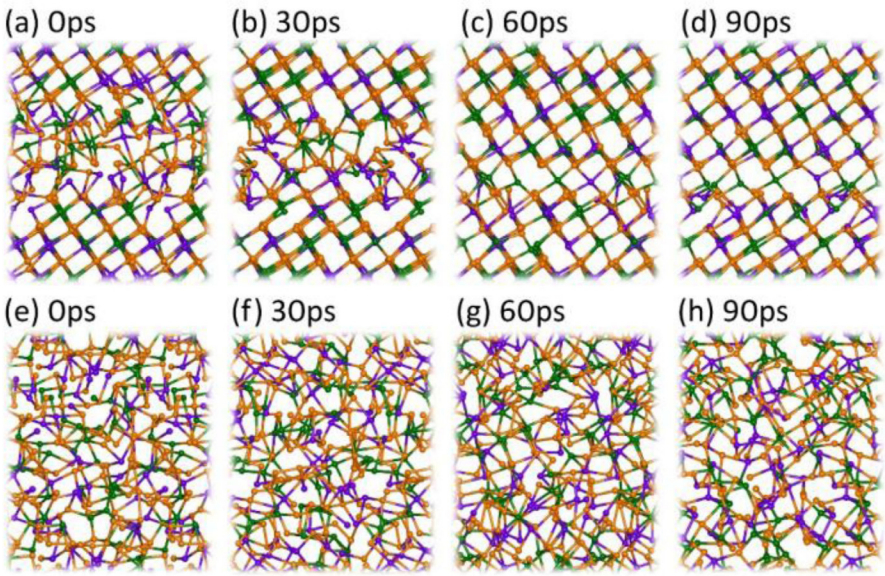

Figure 4. Structural evolution of (a)–(d) iGST and (e)–(h) bGST during recrystallization. Atom color coding is the same as in figure 3.

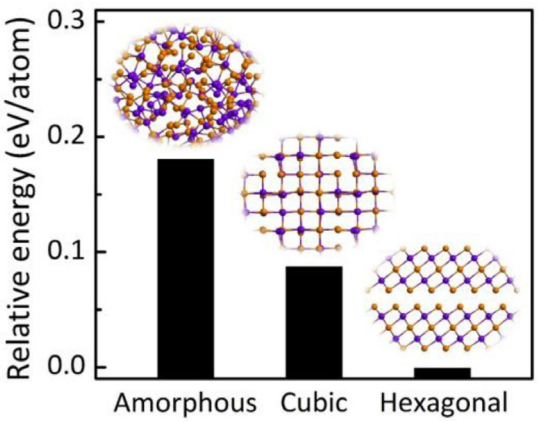

Figure 5. Structures and energies of amorphous, cubic and hexagonal Sb_2Te_3.

and crystalline GST interface at 600 K in a larger calculation cell containing 540 atoms [49]. They also found that crystallization proceeds from the interface instead of nucleation inside the amorphous part, and estimated a fast growth rate of about 1 m s^{-1} due to the high fragility of PCM materials [49, 50]. In addition, such a template effect has been found in the homogeneous amorphous and crystalline interface of other PCM materials such as GeSb and AgInSbTe [50, 51].

To sum up the results of this part: we find in the homogeneous amorphous and crystalline interface structure that the electronic and structural features of the amorphous part become weaker due to the proximity effect of the crystalline part. This will pave the way for crystallization. Furthermore, the crystalline part also provides templates for fast crystallization without a nucleation process. In addition, it can be inferred that the SET speed of PCM materials can be increased by crystalline materials with similar lattice but different components through the amorphous–crystalline interface. For example, very recently, by fabricating a multilayer $TiTe_2/Sb_2Te_3$ heterostructure in which crystalline $TiTe_2$ acts as template and confinement layer, Ding *et al* achieved a PCM device with fast speed as well as ultralow noise and drift [52].

Finally, we also find that the amorphous interface could also stabilize some metastable crystalline phases. Sb_2Te_3 is a basic phase-change material. Its amorphous phase is unstable and will easily transform into a hexagonal crystalline phase at room temperature [53]. Sb_2Te_3 also has a cubic phase with a rock-salt lattice and 33% cation vacancies. Vacancies in cubic Sb_2Te_3 have a random distribution, while in hexagonal Sb_2Te_3 vacancies can be regarded as highly ordered and in the form of van der Waals gaps. It may be thought that cubic and also amorphous Sb_2Te_3 are isotropic. The hexagonal phase is anisotropic. As shown in figure 5, cubic Sb_2Te_3 is a metastable phase and its energy is significantly higher than that of the hexagonal phase (by 88 meV per atom). In fact, the cubic phase has been observed in experiments during the amorphous to hexagonal transition but only exists in quite a small temperature window [54]. We review the results of our former work in figure 6. We find that the stability of metastable cubic Sb_2Te_3 can be enhanced by amorphous GeTe through their interface [29]. Amorphous GeTe and cubic Sb_2Te_3 interface structure are achieved in the deposited GeTe–Sb_2Te_3 (7 nm/6 nm) superlattice-like films, as shown in figure 6(a). The components of the superlattice-like interface structure are confirmed by the EDS mapping in figure 6(b). According to the high-resolution TEM in figure 6(c), GeTe exhibits amorphous features and Sb_2Te_3 has an ordered crystalline structure. The fast Fourier transformation (FFT) clarifies that Sb_2Te_3 has a cubic lattice (see the inset of figure 6(c)). Furthermore, cubic Sb_2Te_3 can remain stable even after heating at 180 °C for 1 min [29]. Compared with the previous experimental work mentioned [54], the stable cubic Sb_2Te_3 here implies its potential application in real PCM devices. It seems that the isotropic feature of the two phases makes cubic Sb_2Te_3 stable.

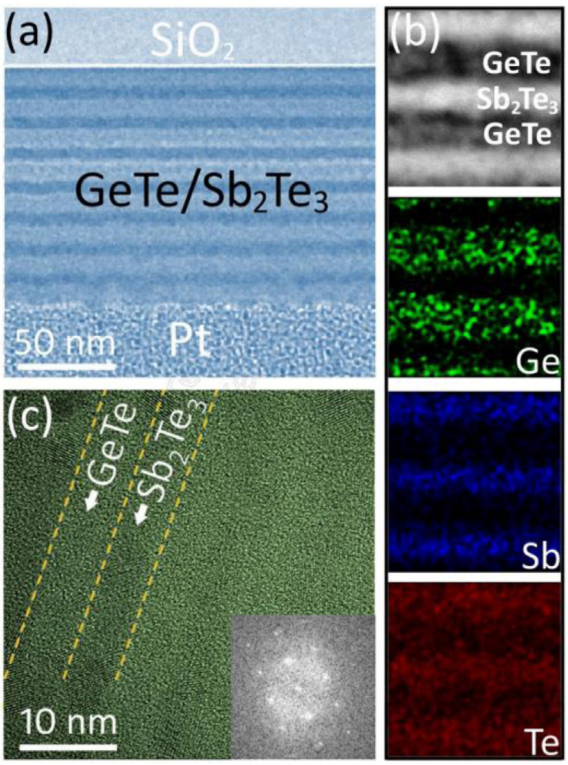

Figure 6. (a) TEM image of a cross-sectional sample of as-deposited $GeTe/Sb_2Te_3$ (7 nm/6 nm) superlattice-like film. (b) High-angle annular dark field scanning transmission electron microscopy image with EDS mapping. (c) High resolution TEM image of superlattice-like structure with the FFT of [0 0 1]-orientated cubic Sb_2Te_3 grain. (a)–(c) Reprinted from [29], Copyright 2019, with permission from Elsevier.

4. Conclusion

In summary, based on the previous results of first-principles calculations and TEM characterizations, we revisit the interface effects on the structural and electronic properties of PCM materials in three typical nano amorphous interfaces. We find that amorphous Si/amorphous Sb_2Te_3 and amorphous GeTe/cubic Sb_2Te_3 interfaces could stabilize amorphous Sb_2Te_3 and metastable cubic Sb_2Te_3, and thus enhance the data retention ability of these materials and also that of devices based on them. In addition, due to the fast crystallization speed of the crystalline/amorphous GST interface, it can be employed to achieve PCM devices with a fast SET speed. We hope that the present study of the interface effect in PCM materials on atomic and electronic scales can support the design and fabrication of novel PCM materials and devices to meet the further requirements of PCM applications.

Acknowledgments

This work was supported by the NSFC (Nos. 61922035, 11904118 and 11874171). The High-performance Computing Venter (HPCC) of Jilin University is also acknowledged for the calculation resources. We acknowledge the invitation to contribute this work to the Special Issue on Phase-Change Memories: Materials Science, Technological Applications and Perspectives.

ORCID iDs

Xue-Peng Wang http://orcid.org/0000-0002-8570-4546
Xian-Bin Li https://orcid.org/0000-0002-0046-2016

References

[1] Ovshinsky S R 1968 *Phys. Rev. Lett.* **21** 1450
[2] Wuttig M and Yamada N 2007 *Nat. Mater.* **6** 824
[3] Fong S W, Neumann C M and Philip Wong H-S 2017 *IEEE Trans. Electron. Devices* **64** 4374
[4] Ríos C, Stegmaier M, Hosseini P, Wang D, Scherer T, David Wright C, Bhaskaran H and Pernice W H P 2015 *Nat. Photon.* **9** 725
[5] Qu Y R, Li Q, Cai L, Pan M Y, Ghosh P, Du K K and Qiu M 2018 *Light Sci. Appl.* **7** 26
[6] Du K K, Li Q, Lyu Y B, Ding J C, Lu Y, Cheng Z Y and Qiu M 2017 *Light Sci. Appl.* **6** e16194
[7] Raoux S, Xiong F, Wuttig M and Pop E 2014 *MRS Bull.* **39** 703
[8] Caravati S, Bernasconi M and Parrinello M 2010 *J. Phys.: Condens. Matter* **22** 315801
[9] Yin X H, Steinle T, Huang L L, Taubner T, Wuttig M, Zentgraf T and Giessen H 2017 *Light Sci. Appl.* **6** e17016
[10] Zhang W, Mazzarello R, Wuttig M and Ma E 2019 *Nat. Rev. Mater.* **4** 150
[11] Skelton J M, Loke D, Lee T and Elliott S R 2015 *ACS Appl. Mater. Interfaces* **7** 14223
[12] Feldmann J, Youngblood N, David Wright C, Bhaskaran H and Pernice W H P 2019 *Nature* **596** 208
[13] Tuma T, Pantazi A, Gallo M L, Sebastian A and Eleftheriou E 2016 *Nat. Nanotechnol.* **11** 693
[14] Simpson R E, Krbal M, Fons P, Kolobov A V, Tominaga J, Uruga T and Tanida H 2010 *Nano Lett.* **10** 414
[15] Mandelli D, Caravati S and Bernasconi M 2012 *Phys. Status Solidi* b **249** 2140
[16] Hayat H, Kohary K and David Wright C 2017 *Nanotechnology* **28** 035202
[17] Sebastian A, Gallo M L, Burr G W, Kim S, BrightSky M and Eleftheriou E 2018 *J. Appl. Phys.* **124** 111101
[18] Zhou X L, Xia M J, Rao F, Wu L C, Li X B, Song Z T, Feng S L and Sun H B 2014 *ACS Appl. Mater. Interfaces* **6** 14207
[19] Rao F, Song Z T, Ren K, Zhou X L, Cheng Y, Wu L C and Liu B 2011 *Nanotechnology* **22** 145702
[20] Wang X P, Chen N K, Li X B, Cheng Y, Liu X Q, Xia M J, Song Z T, Han X D, Zhang S B and Sun H B 2014 *Phys. Chem. Chem. Phys.* **16** 10810
[21] Raoux S, Jordan-Sweet J L and Kellock A J 2008 *J. Appl. Phys.* **103** 114310
[22] Simpson R E, Fons P, Kolobov A V, Fukaya T, Krbal M, Yagi T and Tominaga J 2011 *Nat. Nanotechnol.* **6** 501
[23] Li X B, Chen N K, Wang X P and Sun H B 2018 *Adv. Funct. Mater.* **28** 1803380
[24] Zhu M *et al* 2014 *Nat. Commun.* **5** 4086
[25] Rao F *et al* 2017 *Science* **358** 1423

[26] Rao F, Zong Z T, Cheng Y, Liu X S, Xia M J, Li W, Ding K Y, Feng X F, Zhu M and Feng S L 2015 *Nat. Commun.* **6** 10040
[27] Hohenberg P and Kohn W 1964 *Phys. Rev.* **136** B864
[28] Wang X P, Li X B, Chen N K, Chen Q D, Han X D, Zhang S B and Sun H B 2017 *Act Mater.* **136** 242
[29] Chen Y J, Wang X P, Zhang Q, Deng Q S, Li X B, Zhang B, Zhang Z and Han X D 2019 *Mater. Lett.* **243** 153
[30] Kresse G and Joubert D 1999 *Phys. Rev.* B **59** 1758
[31] Kresse G and Furthmuller J 1996 *Phys. Rev.* B **54** 11169
[32] Perdew J P, Burke K and Ernzerhof M 1997 *Phys. Rev. Lett.* **78** 1396
[33] Nośe S 1991 *Prog. Theor. Phys. Suppl.* **103** 1–46
[34] Custer J S, Tompson M O, Jacobson D C, Poate J M, Roorda S, Sinke W C and Spaepen F 1994 *Appl. Phys. Lett.* **64** 437
[35] Shportko K, Kremers S, Woda M, Lencer D, Roberson J and Wuttig M 2008 *Nat. Mater.* **7** 653
[36] Zhu M, Cojocaru-Mirédin O, Mio A M, Keutgen J, Küpers M, Yu Y, Cho J-Y, Dronskowski R and Wuttig M 2018 *Adv. Mater.* **30** 1706735
[37] Chen N K, Li X B, Wang X P, Tian W Q, Zhang S B and Sun H B 2018 *Acta Mater.* **143** 102
[38] Savin A, Jepsen O, Flad J, Andersen O K, Preuss H and von Schnering H G 1992 *Angew. Chem., Int. Ed. Engl.* **31** 187
[39] Caravati S, Bernasconi M, Kühne T D, Krack M and Parrinello M 2007 *Appl. Phys. Lett.* **91** 171906
[40] Zhang B *et al* 2016 *Sci. Rep.* **6** 25453
[41] Ross U, Lotnyk A, Thelander E and Rauschenbach B 2014 *Appl. Phys. Lett.* **104** 121904
[42] Kolobov A V, Fons P, Frenkel A I, Adkudinov A L, Tominage J and Uruga T 2004 *Nat. Mater.* **3** 703
[43] Zhang W, Deringer V L, Dronskowsk R, Mazzarello R, Ma E and Wuttig M 2015 *MRS Bull.* **40** 856
[44] Li X B, Liu X Q, Liu X, Han D, Zhang Z, Han X D, Sun H B and Zhang S B 2011 *Phys. Rev. Lett.* **107** 015501
[45] Errington J R and Debenedetti P G 2011 *Nature* **409** 318
[46] Lee T H and Elliott S R 2011 *Phys. Rev. Lett.* **107** 145702
[47] Ourmazd A, Bean J C and Phillips J C 1985 *Phys. Rev. Lett.* **55** 1955
[48] Lee T H and Elliott S R 2011 *Phys. Rev.* B **84** 094124
[49] Ronneberger I, Zhang W, Eshet H and Mazzarello R 2015 *Adv. Funct. Mater.* **25** 6407
[50] Zhang W, Ronneberger I, Zalden P, Xu M, Salinga M, Wuttig M and Mazzarello R 2014 *Sci Rep.* **4** 6529
[51] Hegedus J and Elliott S R 2010 *Phys. Status Solidi* a **3** 510
[52] Ding K Y, Wang J J, Zhou Y X, Tian H, Lu L, Mazzarello R, Jia C L, Zhang W, Rao F and Ma E 2019 *Science* **366** 210
[53] Arun P, Tyagi P, Vedeshwar A G and Paliwal V K 2005 *Physica* B **307** 105
[54] Zheng Y H, Xia M J, Cheng Y, Rao F, Ding K Y, Liu W L, Jia Y, Song Z T and Feng S L 2016 *Nano Res.* **9** 3453